The Impact of Thermoelectric Leg Geometries on Thermal Resistance and Power Output

Yohann Thimont[1], Saniya LeBlanc[2*]

[1]Université Paul SABATIER CIRIMAT, 118, Route de Narbonne, 31062 Toulouse, France
[2] Department of Mechanical and Aerospace Engineering, The George Washington University, 800 22nd St. NW, Washington, DC 20052, USA

*Corresponding author email address: sleblanc@gwu.edu

Abstract

Thermoelectric devices enable direct, solid-state conversion of heat to electricity and vice versa. Rather than designing the shape of thermoelectric units or legs to maximize this energy conversion, the cuboid shape of these legs has instead remained unchanged in large part because of limitations in the standard manufacturing process. However, the advent of additive manufacturing (a technique in which freeform geometries are built up layer-by-layer) offers the potential to create unique thermoelectric leg geometries designed to optimize device performance. This work explores this new realm of novel leg geometry by simulating the thermal and electrical performance of various leg geometries such as prismatic, hollow, and layered structures. The simulations are performed for two materials, a standard bismuth telluride material found in current commercial modules and a higher manganese silicide material proposed for low cost energy conversion in high temperature applications. The results include the temperature gradient and electrical potential developed across individual thermoelectric legs as well as thermoelectric modules with sixteen legs. Even simple hollow and layered leg geometries result in larger temperature gradients and higher output powers than the traditional cuboid structure. The clear dependence of thermal resistance and power output on leg geometry provides compelling motivation to explore additive manufacturing of thermoelectric devices.

I. Thermoelectrics Overview

Thermoelectric devices provide the ability to convert heat into electricity or pump heat, so they have applications in both power generation and localized heating/cooling. As solid-state devices, they have no moving parts. The structure of a conventional thermoelectric device is depicted in Figure 1. Individual units of thermoelectric material (often referred to as “legs” or “pins”) are connected electrically in series and thermally in parallel. The legs are physically attached to electrical connectors arranged on electrically insulating ceramic plates. The resulting device unit is called a thermoelectric module. Thermoelectric modules are often integrated into heat exchangers to interface with a heat source or coolant.

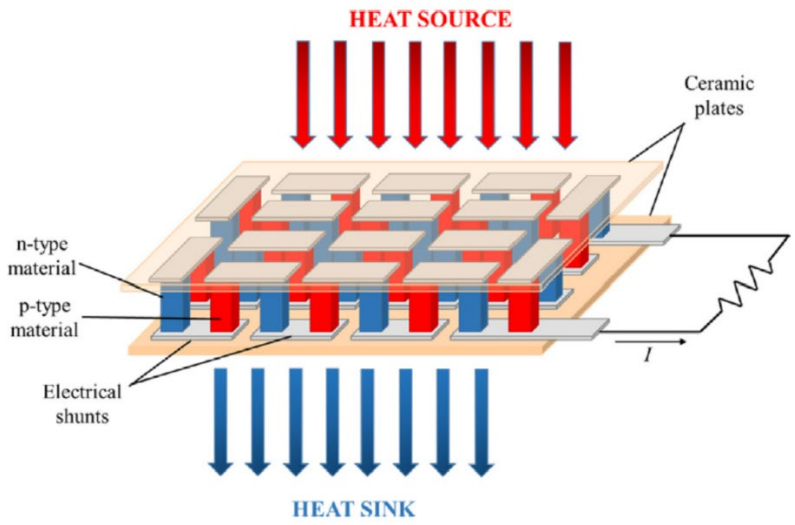

Figure 1. Schematic of a conventional thermoelectric module. Reproduced with permission from J. of Manufacturing Processes 25 (2017). Copyright 2017 Elsevier [1].

As solid-state energy conversion devices, thermoelectric device performance hinges on the Seebeck effect in the active thermoelectric materials. The Seebeck coefficient S is a material property which denotes the ratio of the electrical potential to the temperature gradient across the material, so a high Seebeck coefficient is favorable. As such, n- and p-type degenerate semiconductor materials with high S are typically grouped in coupled legs. In order to maintain a large temperature gradient across the material and facilitate electrical carrier transport through it, low thermal conductivity k and high electrical conductivity σ are desirable intrinsic thermoelectric material properties. There have been detailed reviews of the physics and design of thermoelectric materials [2]–[4], and there has been some work investigating the impact of thermoelectric leg design on module performance. The following section describes prior investigations about the impact of geometric and system-level parameters on thermal management and thus device performance.

A. Thermal Resistance Considerations

Designing the thermal resistance of individual legs as well as the collection of legs in a module is critical to thermoelectric device design because the temperature gradient across the thermoelectric legs directly determines the electrical potential which develops across the legs. These thermal resistances impact the device efficiency and power output. In a simple, 1D, steady-state heat transfer model of a thermoelectric device, the temperature gradient ΔT across the device is proportional to the heat transfer rate q through the device and the thermal resistance R_t of the device: $\Delta T = qR_t$. The thermal resistance is composed of both intrinsic material properties and extrinsic properties such as geometric dimensions, and each component or feature of the device has an associated thermal resistance, resulting in a thermal resistance network for the overall device. The impact of these thermal resistances on system performance has been investigated and resulted in various insights about designing the thermal resistance of the thermoelectric module relative to the thermal resistance of the other system components [5]–[10].

The thermal resistance of the module depends heavily on the thermal resistance of the legs. Analyses of individual leg resistances and thermal interactions between legs have focused largely on optimal leg aspect ratio and fill factor (the proportion of a thermoelectric device's area which is occupied by thermoelectric material). The typical leg geometry is a cuboid in which the leg has a rectangular cross-section whose area is the same for the entire leg length. The cuboid geometry causes practical challenges in thermoelectric device design and optimization. Since the material properties are temperature-dependent, and the properties of n- and p-type materials in the same device differ from each other, the optimal length and cross-sectional area of the n- and p-type legs might not match. Given the conventional device geometry depicted in Figure 1, variations in length are impractical since all legs must be the same length. Segmented or cascaded legs overcome this limitation to some extent since they enable customized design of the leg material properties in relation to the temperature at each point along the leg [11]–[15]. Often, module designers will determine the optimum fill factor and/or leg aspect ratio to optimize device performance (e.g., maximize efficiency or power output) [16]–[19]. One of the critical challenges in thermoelectric device reliability stems from the differing thermal expansion coefficients between the various thermoelectric materials and the metal electrical connectors to which the legs adhere. The coefficient of thermal expansion variation leads to regions of high stress and oftentimes cracking. An innovative approach to overcome challenges with leg length, cross-sectional area, and thermal expansion differences involved an alternative connector shape. A "Y" shaped connector sandwiched between the n- and p-type legs changed the orientation of the electrical connectors with respect to the legs and overcame some of the critical challenges posed by the conventional device geometry [20].

In spite of the extensive work on thermoelectric material and device development, there has been limited consideration of alternative leg geometries, beyond conventional cuboid shapes of the same length. Cylindrical legs have been made to wrap around curved surfaces, namely pipes carrying a hot fluid [21]–[23]. More recent work demonstrated the impact of alternative geometries through which the fill factor could be greater than 1, and a prototype of printed, thick film thermoelectric elements in circular geometries was created [24], [25]. Patents issued over a decade ago describe the potential of legs with varying lengths and cross-sections within a module [26], [27]. Theoretical analysis of trapezoidal leg geometries indicates these geometries can lead to higher device efficiency [28]–[30].

B. Manufacturing Influences on Leg Geometry

If influencing the thermoelectric leg and device thermal resistances is so heavily dependent on leg geometry, why then are leg geometries so limited? The answer reveals an underlying limitation to the development of thermoelectric devices. The leg and device geometries have been dictated largely by the conventional device manufacturing process which limits the leg shape to a cuboid geometry [31]. Indeed, the study of trapezoidal leg geometries presents the concept of changing leg width as a function of leg length, but it cites manufacturing feasibility as a justification for considering only trapezoidal geometries [28].

Recent work indicates these manufacturing limitations could be overcome. Additive manufacturing – building a part layer-by-layer – provides the ability to make freeform shapes and removes many of the geometric constraints of conventional, subtractive manufacturing processes. Although additive manufacturing (colloquially known as 3D printing) has been become prolific, its application to thermoelectric materials and devices is relatively new.

Additive manufacturing techniques have been shown on multiple low- and high-temperature thermoelectric materials such as bismuth telluride [1], [32]–[36], higher manganese silicide [37], half-Heusler [38], and skutterudite [39], thus demonstrating the feasibility of the manufacturing approach for these semiconductor materials. These advances in manufacturing capability open the door to a myriad of thermoelectric leg geometries which were previously unrealistic: a new frontier in thermoelectric leg design is open.

This work aims to embark on the exploration of this frontier. We simulate traditional (square/cuboid, cylindrical), previously proposed (trapezoidal), and entirely new (triangular, hollow, layered) leg geometries. While not optimized for any particular performance metric, the layered leg geometries showcase the capability of additive manufacturing over traditional manufacturing mechanisms. In a subtractive manufacturing approach, the layered geometry would be practically untenable since it would require individually milling every leg or stacking leg units together (and thus introducing detrimental thermal and electrical interface resistances). The modeling results demonstrate the impact of leg geometry on temperature gradients, thermal resistance, and electrical potential for both individual legs and a module with several legs. Both low and high temperature scenarios are modeled using bismuth telluride and higher manganese silicide legs.

II. Modeling Approach

The impact of individual leg geometry on thermal resistance was investigated with a finite element method analysis implemented with a tetrahedron polygon mesh in COMSOL Multiphysics software. The adaptive mesh feature in COMSOL was used to determine the mesh size for each leg geometry. Between 6 and 10 tetrahedra along the leg's z-axis were used to calculate the temperature and voltage gradients, and each tetrahedron is 0.7-1.2 mm long. Four basic leg geometries were investigated. In the discussion, they will be referred to as triangular, square, circular, and trapezoidal in reference to their nominal shape. Three variations of the geometries were investigated: filled, hollow, and layered. Figure 2 shows these leg geometric variations. The filled square geometry is typical and represents what is found in most commercial modules; however, conventional modules sometimes have legs with rectangular cross-sections where the cross-sectional dimensions are selected to optimize performance. Since recent studies have investigated the trapezoidal geometry as a representation of varying the cross-section along the leg length, the trapezoidal geometry is also modeled here, enabling comparison between our results and this proposed geometry. The trapezoidal geometry was modeled only in a filled variation, per the prior studies, but the orientation of the trapezoid was varied. The small and large bases of the trapezoidal legs have dimensions of 2x2 mm^2 and 4x4 mm^2, respectively. The volume of each leg was fixed at 63 mm^3 and does not vary between leg geometries. With the exception of the trapezoidal geometries, the surface area at the constant temperature boundary was held constant. Table 1 presents the legs' projected area (equivalent to the largest cross-sectional area along the leg's length) and the total surface area.

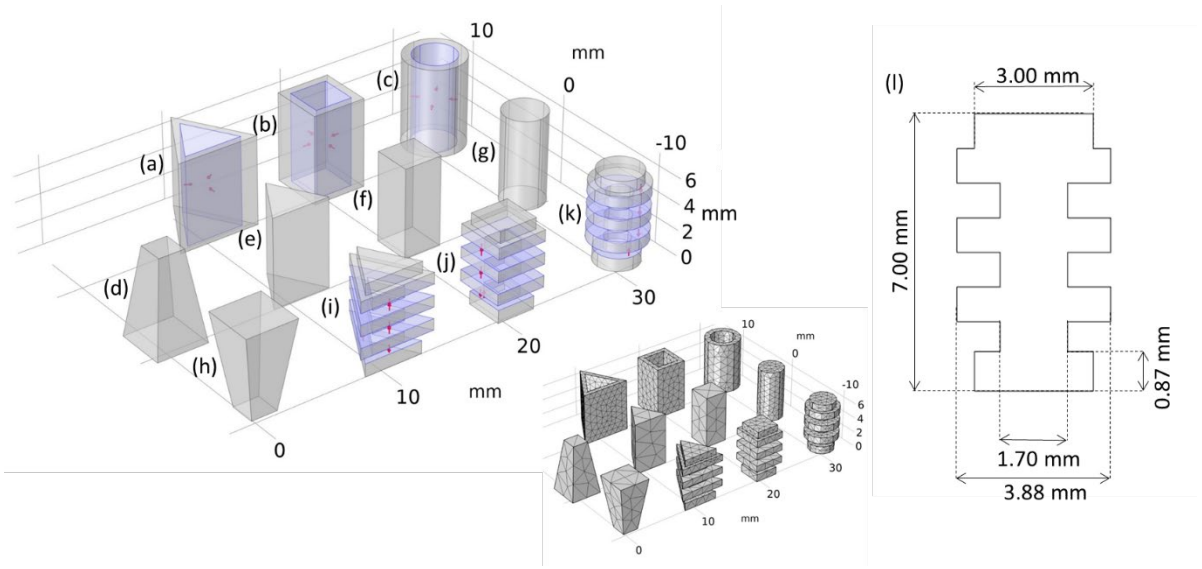

Figure 2. Schematic of leg geometries modeled where the geometries are: (a) triangular (hollow), (b) square (hollow), (c) circular (hollow), (d) trapezoidal (large base), (e) triangular (filled), (f) square (filled), (g) circular (filled), (h) trapezoidal (small base), (i) triangular (layered), (j) square (layered), (k) circular (layered). The square (filled) geometry (f) approximates the conventional leg geometry. Arrows show the normal to the surface for the purposes of the radiation analysis. The inset shows the adaptive meshing used. (l) Schematic cross-section of the square layered geometry.

Table 1. Projected area (in mm^2) for the leg geometries modeled; the leg total surface area values, including interior surfaces which face other surfaces, are shown in parentheses. For the trapezoidal cross-section, the area values are the same regardless of the leg orientation (i.e., large or small base).

Vertical Classification	**Nominal Classification**			
	Triangular	**Square**	**Circular**	**Trapezoidal**
Hollow	18 mm^2 (270.8)	18 (220.8)	18 (197.7)	
Filled	9 (113.7)	9 (102.0)	9 (92.4)	16 (104.9)
Layered	15 (182.4)	15 (170.9)	15 (161.5)	

A constant temperature boundary condition was applied to the bottom surface of the geometries. The bottom side is the "hot side," and the top surface is the "cold side." For the individual leg simulations, the top surface boundary condition is a radiative heat flux condition. In the module simulations, the legs' top surfaces are connected to metal shunts. There is heat conduction from the leg to the metal shunt, and there is a radiative heat flux condition from the top of the metal shunt. In all simulations, the steady-state analysis accounted for heat conduction within the leg and the electrical potential developed across the leg due to the Seebeck effect. Heat conduction is determined by Fourier's law:

$$\vec{q} = -k\nabla T \qquad (1)$$

where $\vec{q}$ is the heat flux vector, and k is the thermal conductivity of the material. The electrical potential at each node was determined with the Seebeck relationship:

$$\vec{E} = S \times \vec{\nabla} T \qquad (2)$$

where $\vec{E}$, S, and T are the vector of the electric field intensity (or gradient of the electrical potential), Seebeck coefficient, and temperature, respectively. The open circuit voltage V_{oc} was determined from the Seebeck effect and temperature gradient. The maximum current density is

$$\left|\vec{J}_{max}\right| = \frac{I_{max}}{A} = \sqrt{\left|\vec{J}_{x,max}\right|^2 + \left|\vec{J}_{y,max}\right|^2 + \left|\vec{J}_{z,max}\right|^2} \qquad (3)$$

where A is the cross-sectional area of the leg at a given position, and $J_{x,max}$, $J_{y,max}$, $J_{z,max}$ are the current density tensor components as a given position. The maximum current density was obtained by modeling the leg under a short circuit condition. The internal electrical resistance of the leg, R_{int}, is V_{oc}/I_{max}. The voltage across each leg, U, as a function of the current through the leg, I, is

$$U = V_{oc} - IR_{int} \qquad (4)$$

The output power of the leg, P, is then

$$P = IU = IV_{oc} - I^2 R_{int} \qquad (5)$$

The area-normalized output power was calculate as P/A_{max} where A_{max} is the maximum projected area (the area projected onto the base plane).

Two materials were modeled: bismuth telluride and higher manganese silicide (HMS). The former is a standard, low temperature thermoelectric material found in the majority of off-the-shelf thermoelectric devices. The results for bismuth telluride legs and modules enable the reader to compare this work's results with those of other studies which have investigated versions of the filled square geometry (Figure 2f). On the other hand, HMS is a newer material targeted at mid- to high-temperature operating conditions, and it is potentially lower cost than alternative materials because it is composed of readily available elements. For the model, the intrinsic, temperature-dependent material properties from experimental measurements were used. Experimental details for HMS ($MnSi_y$ where $1.73<y<1.77$), including its emissivity, are reported elsewhere [40], and the temperature-dependent functional forms of the Seebeck coefficient, electrical conductivity, and thermal conductivity valid for the temperature range 30°C to 530°C are as follows:

$$S\left[V \times K^{-1}\right] = -1.76 \times 10^{-5} + 5.63 \times 10^{-7} T - 3.27 \times 10^{-10} T^2 \qquad (6)$$

$$\sigma\left[S \times m^{-1}\right] = -7.82 \times 10^{4} - 128.17 \times T + 7.45 \times 10^{-2} \times T^2 \qquad (7)$$

$$k\left[W \times m^{-2} \times K^{-1}\right] = 4.79 - 4.82 \times 10^{-3} \times T + 2.96 \times 10^{-6} \times T^2 \qquad (8)$$

The properties for bismuth telluride were extracted from [2] where the measured properties for n-type $Bi_2Te_{2.7}Se_{0.3}$ and p-type $Bi_{0.5}Sb_{1.5}Te_3$ are reported. The n-type material properties were used for the single leg results reported here, and the functional forms valid for the temperature range -100°C to 70°C are provided below:

$$S[V \times K^{-1}] = -3.18 \times 10^{-5} - 9.73 \times 10^{-7} \times T + 1.14 \times 10^{-9} \times T^2 \quad (9)$$

$$\sigma\left[S \times m^{-1}\right] = 450156.76 - 1988.01 \times T + 2.64 \times T^2 \quad (10)$$

$$k\left[W \times m^{-1} \times K^{-1}\right] = 4.33 - 1.74 \times 10^{-2} \times T + 2.64 \times 10^{-5} \times T^2 \quad (11)$$

The properties were treated as isotropic properties. A constant temperature thermal boundary condition of 400°C and 70°C was applied to the hot side of the HMS and bismuth telluride legs, respectively.

Radiative heat transfer was incorporated in the individual leg models; radiation between surfaces existing on each leg were considered. For example, in a hollow leg structure, the radiation between interior surfaces was modeled. The surfaces for which radiation in individual legs were considered are indicated in Figure 2 with arrows orthogonal to the relevant surfaces. Adaptive meshing was used to resolve the surface-to-surface radiation. The mesh in the space between surfaces results in a spatial resolution of approximately 1 mm^2 (the mesh tetrahedron size). Heat transfer by radiation was modeled with the Stefan-Boltzmann law:

$$\vec{n} \cdot q_{rad} = \varepsilon \sigma_s (T^4 - T_\infty^4) \quad (12)$$

where $\vec{n}$ is the normal vector to the boundary, ε is the emissivity of the material, σ_s is the Stefan-Boltzmann constant, T is the temperature of the meshed domain, and T_∞ is the ambient temperature set as 20°C. For HMS, the emissivity was measured experimentally at 0.6 [40]. The emissivity of bismuth telluride was taken as 0.66 from [41], but this material property is not widely characterized for thermoelectric materials, even a common one such as bismuth telluride.

In addition to analyzing individual legs, the thermal interaction between legs was investigated using a module geometry consisting of eight leg couples where each couple has a p- and n-type leg. Many modules are evacuated, particularly to avoid oxidation in modules operating at mid- to high-temperatures. The models presented here consider vacuum conditions, so radiative heat transfer between the legs was considered in addition to radiation between the surfaces on each leg (i.e, between the layer surfaces of the layered geometry). In some devices, the space between the legs is filled in an insulating foam, and radiative heat transfer would not be present. In those cases, the temperature gradient across the legs would be larger than that predicted in this simulation, and the variation between legs in a given module would not be present.

The module simulations were conducted for a module with 8 legs of p-type Bi-doped HMS and 8 legs of n-type Bi-doped Mg_2Si, so the module consisted of 8 couples where each couple had one p-type and one n-type leg. The module was modeled with the thermoelectric legs adhered to metal connectors (copper) using a metallic braze material (nickel). The electrical contact resistance of this braze contact between the thermoelectric material and the metal shunt was included in the model according the values measured experimentally [42]. New thermoelectric modules that enable adaptive design have been made without a top substrate [43]. This design reduces the mechanical stress induced in the thermoelectric material due to the differences in thermomechanical properties (e.g., coefficient of thermal expansion) of the substrate, metal shunts, and thermoelectric materials [40]. The reduction of mechanical stress in thermoelectric modules improves reliability, particularly in applications with thermal cycling. The reduced-substrate research and development advancement is incorporated in these module

simulations; there is no top (cold side) substrate. Therefore, there is no hot-to-cold substrate radiation, and the absence of this radiation component further emphasizes the temperature gradients resulting from changes in the leg geometry.

III. Results

A. Single Leg Results

The influence of leg geometry on the resulting temperature gradient, Seebeck voltage, and current was determined. Figure 3 shows the temperature gradient and open circuit electrical potential, $V_{OC,}$ for legs of each geometry and two types of materials, HMS and $Bi_2Te_{2.7}Se_{0.3}$. The results for all of the legs are shown in each figure panel; however, the legs were modeled individually, not collectively as a module. Table 2 reports the temperature gradient across the leg as well as the gradient normalized by the leg's projected area. Because the model incorporates each material's temperature-dependent thermal conductivity, and the cross-sectional area of the layered legs vary as a function of leg length, there is no direct relationship for determining the leg thermal resistance in the manner described in section I. However, the temperature gradient and area normalized temperature gradient provide a conceptual understanding of the resistance to heat transfer, particularly comparing relative values between legs of different geometries.

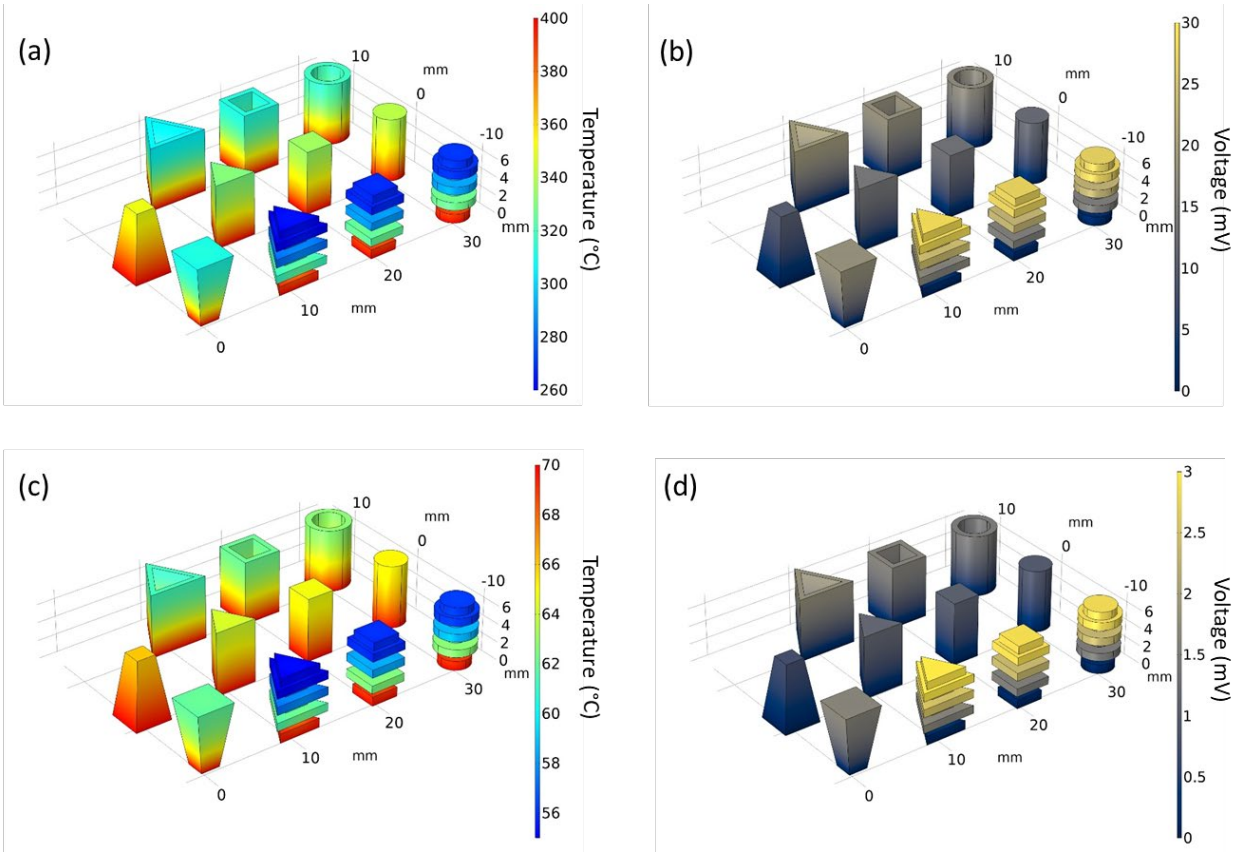

Figure 3. Gradients in temperature and electrical potential along thermoelectric legs of different geometries; the "hot side" is at the bottom of the legs. Top panels (a) and (b) show the results for

higher manganese silicide. Bottom panels (c) and (d) show the results for bismuth telluride. Figures (a) and (c) show the surface temperature variation along the length of the leg. Figures (b) and (d) show the surface electrical potential (in open circuit) resulting from the Seebeck effect.

Table 2. Temperature gradient across each leg (in °C); the area normalized temperature gradient (in °C/mm^2) is reported in parentheses. The latter is the temperature gradient divided by the projected area reported in Table 1. The values for all leg geometries and both materials, higher manganese silicide (HMS) and bismuth telluride (where BT abbreviates $Bi_2Te_{2.7}Se_{0.3}$), are reported. The conventional cuboid geometry is outlined in bold to enable comparison of the novel geometries to the standard one. The temperature gradients for HMS and BT were determined using the hot side temperatures of 400°C and 70°C, respectively.

	Triangular		**Square**		**Circular**		**Trapezoidal (large base)**		**Trapezoidal (small base)**	
	HMS	**BT**	**HMS**	**BT**	**HMS**	**BT**	**HMS**	**BT**	**HMS**	**BT**
Hollow	94°C (5.2°C/mm^2)	8.7 (0.48)	87 (4.9)	7.9 (0.44)	82 (4.6)	7.3 (0.40)				
Filled	69 (7.7)	5.8 (0.65)	64 (7.1)	5.3 (0.59)	60 (6.6)	4.8 (0.54)	50 (3.1)	3.9 (0.24)	88 (5.5)	8.0 (0.50)
Layered	138 (9.2)	15 (0.99)	132 (8.8)	14 (0.94)	130 (8.7)	14 (0.92)				

The leg geometry noticeably influences the temperature difference and electrical potential across the leg. In spite of the surface-to-surface radiation present within the hollow and layered geometries, the heat transfer rate is lower in the hollow and layered geometries compared to their filled counterparts. The effective thermal resistance of the hollow and layered geometries are higher than those of their filled counterparts. In particular, the temperature gradients across layered leg geometries are even larger than those for the other geometries despite the radiative heat transfer between the multiple layers of the layered geometries. The pronounced enhancement (an increase in thermal resistance) due to the layered structure stems from the impact of the leg geometry on the thermal resistance. Since the electrical potential directly relates to the temperature gradient, these thermal trends extend to the open circuit voltage developed across each of the leg geometries.

Generally, the temperature difference across the triangular leg is larger than that across the conventional square leg which is larger than that across the cylindrical geometry. For the trapezoidal shape, the orientation with the small base (smaller cross-section at the hot side) results in a larger temperature gradient than the large base orientation. The trapezoidal shape was previously modeled with constant properties without incorporating the temperature dependence of the thermoelectric material properties [28]. To investigate the impact of the properties' temperature dependence on the temperature gradient across the leg, we also conducted the simulation with constant properties where the properties were taken at the average temperature (the average of the maximum and minimum temperatures). For the large base trapezoidal leg, the temperature gradients for the temperature-dependent and constant properties scenarios were 50°C and 49°C, respectively. For the small base trapezoidal leg, the temperature gradients for the temperature-dependent and constant properties scenarios were 88°C and 87°C, respectively. This comparison demonstrates the leg geometry impacts the temperature gradient more than the temperature dependence of the material properties.

The electrical resistance is also relevant in comparing the various geometries because changes in cross-sectional area leading to higher thermal resistance necessarily increase electrical resistance. Additionally, the electrical resistivity is temperature dependent. Dividing the open circuit voltage by the short circuit current yields the electrical resistance; it is the slope of the voltage versus current plot shown in Figure 4. For legs with the filled cross-section, the electrical resistances are similar since the cross-sectional areas of these legs are the same. However, the V_{oc} of the square leg is lower than that of the triangular leg, and the V_{oc} of the circular leg is the lowest. The V_{oc} variation results from the temperature gradients discussed above. Since the cross-sectional area for current transport is the same for hollow geometries as for the filled ones, the electrical resistances of the hollow geometries are similar. The hollow geometries have slightly higher V_{oc} values, again due to the variation in thermal gradients across the legs. The relevant cross-sectional area for current transport varies along the leg length for the layered geometries. Since there are regions of smaller cross-sectional area, the resistances of the layered legs are higher than the other geometries which is also consistent with the thermal resistance results. The trapezoidal geometries have higher internal resistances than the conventional square filled geometry. The trapezoidal leg with the small base has a similar V_{oc} as the hollow legs (which is significantly higher than that of the filled legs), but the layered legs have the highest V_{oc}.

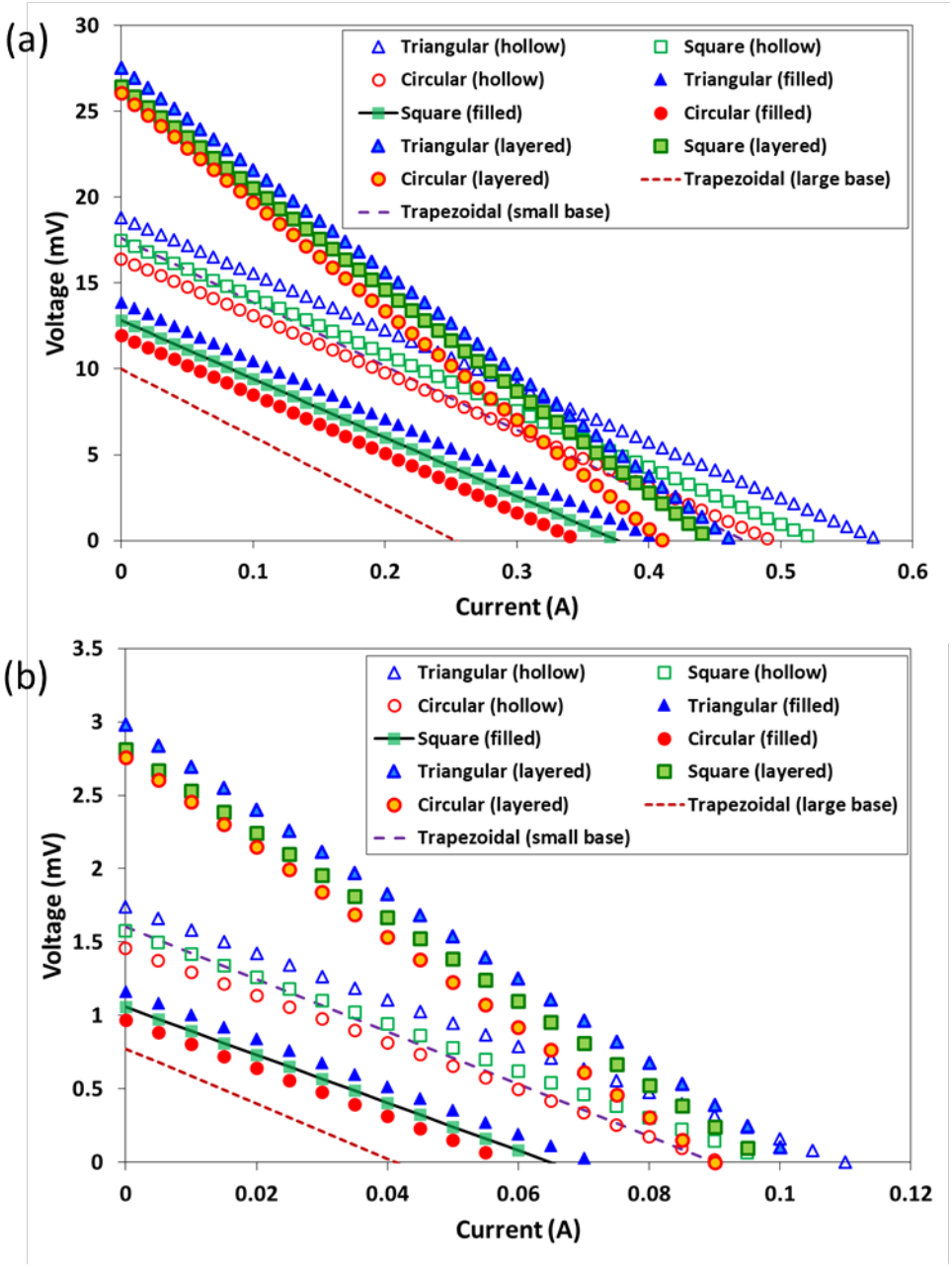

Figure 4. Open circuit voltage and short circuit current for each leg geometry for (a) higher manganese silicide and (b) bismuth telluride. The slope of each line yields the electrical resistance of the leg. The square (filled) geometry most closely resembles the conventional leg geometry.

The theoretical power output for each leg geometry was determined as a function of electrical current, and the values are reported in Figure 5a. The output electrical power is higher for the triangular leg compared to the square and cylindrical legs because there is a larger temperature difference across the triangular leg but minimal change in electrical resistance. The variation in electrical resistance occurs due to the variation of resistivity with temperature; the cross-sectional areas of the filled geometries are the same. The trapezoidal shape with the small base yields higher output power compared to the filled square leg. The hollow geometries result

in higher output electrical power than the filled geometries, and the layered geometries show the highest benefit in terms of output electrical power.

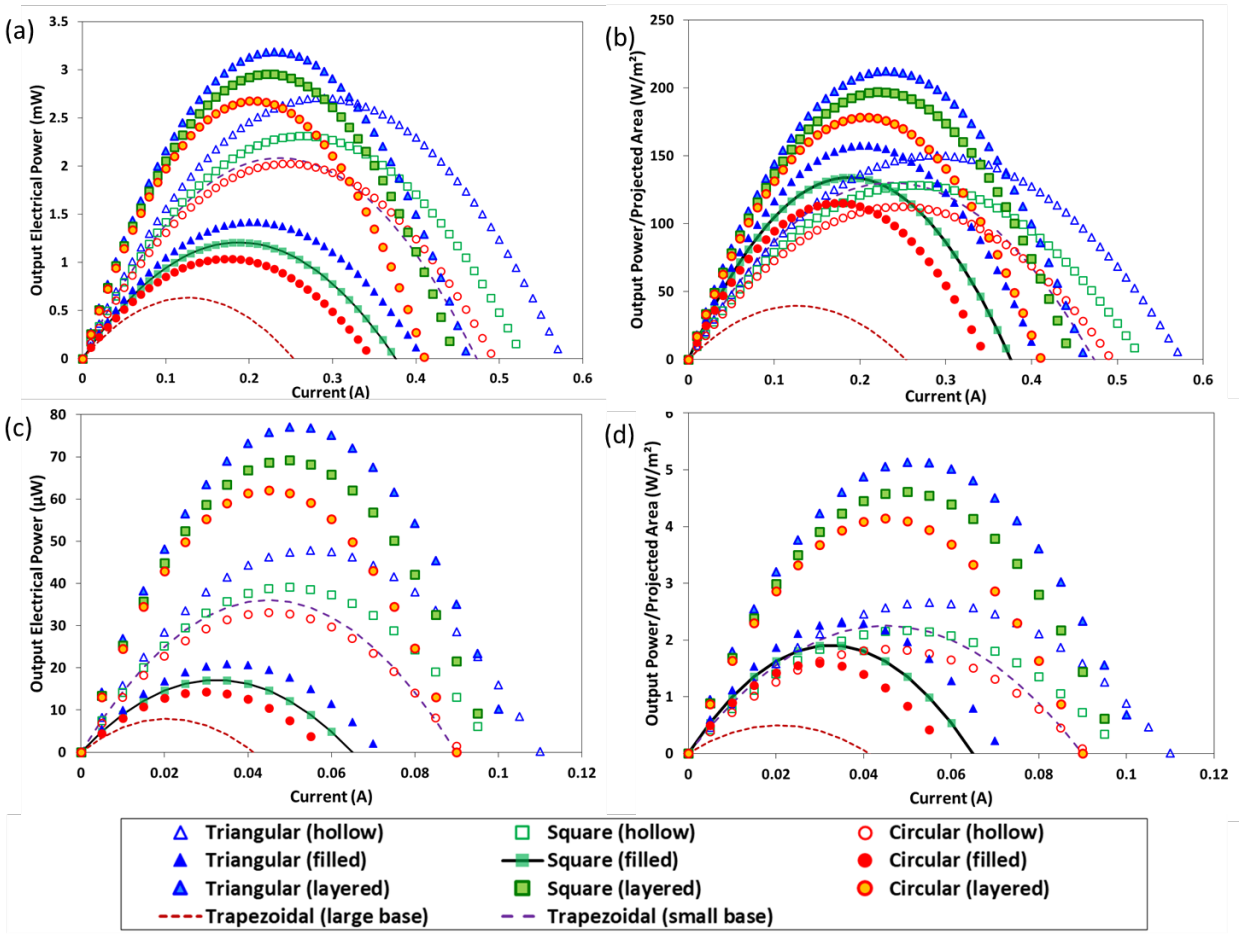

Figure 5. Output electrical power for legs made of (a,b) higher manganese silicide and (c,d) bismuth telluride. (a,c) Output electrical power as a function of the electrical current for the various leg geometries. (b,d) Output electrical power normalized by the leg's projected area as a function of electrical current for various leg geometries.

Areal power density is a useful metric because it normalizes the electrical power output by the surface area the thermoelectric module would consume. For individual legs where the cross-sectional area varies along the length of the leg, the relevant area is the maximum cross-sectional area (including hollow regions), or the projected area, because this area would determine the minimum sizing of the thermoelectric module. Figure 5b shows the areal power density – the power divided by the projected area – in W/m² for the various geometries. In contrast to the comparisons for the peak output power, the peak areal power densities for filled and hollow geometries are similar. The trapezoidal shape has low areal power density, even lower than the conventional filled square shape. This result is in agreement with the conclusion of [30]. The layered geometries have the highest areal power density, with maximum areal power densities that are 35-55% higher than their filled counterparts.

B. Module Results

The impact of leg geometry on a collection of legs in a thermoelectric module is depicted in Figure 6 for the HMS material. Figures 6a-b show the results for a conventional (square, filled) leg geometry while Figures 6c-d show the results for the square, layered leg geometry. The results show the strong influence of surface-to-surface heat radiation which leads to higher temperatures on the top (cold side) of the four legs which are located in the middle of the thermoelectric module. Even in the presence of radiation between the legs, the high thermal resistance of the layered leg geometry shows significant benefit with a larger temperature gradient across all the legs compared to the conventional geometry. The high thermal conductivity of the metal electrical connectors on the top causes them to act as thermal shunts which pull heat from the center to the edges of the module.

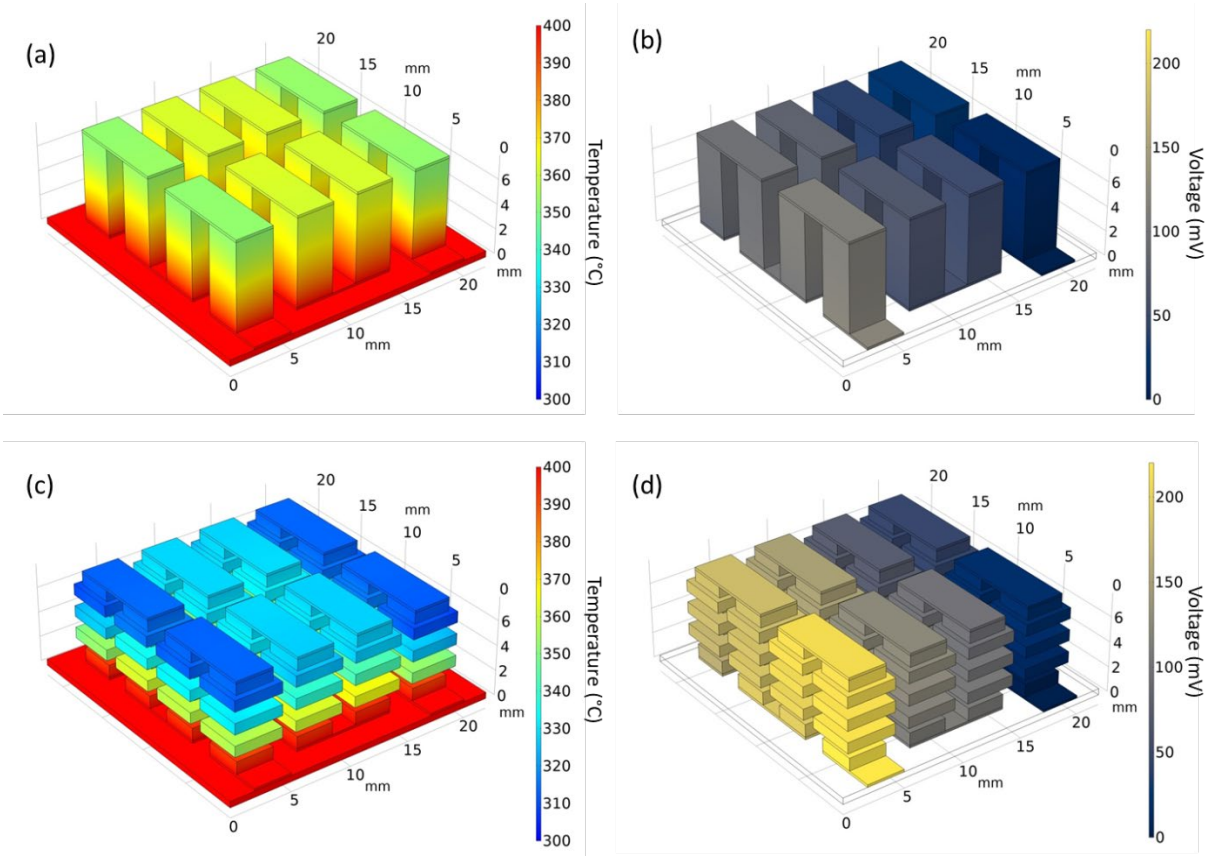

Figure 6. Module simulation results showing gradients in (a, c) temperature and (b, d) electrical potential for modules with (a,b) conventional and (c,d) layered leg geometries where the legs are composed of HMS.

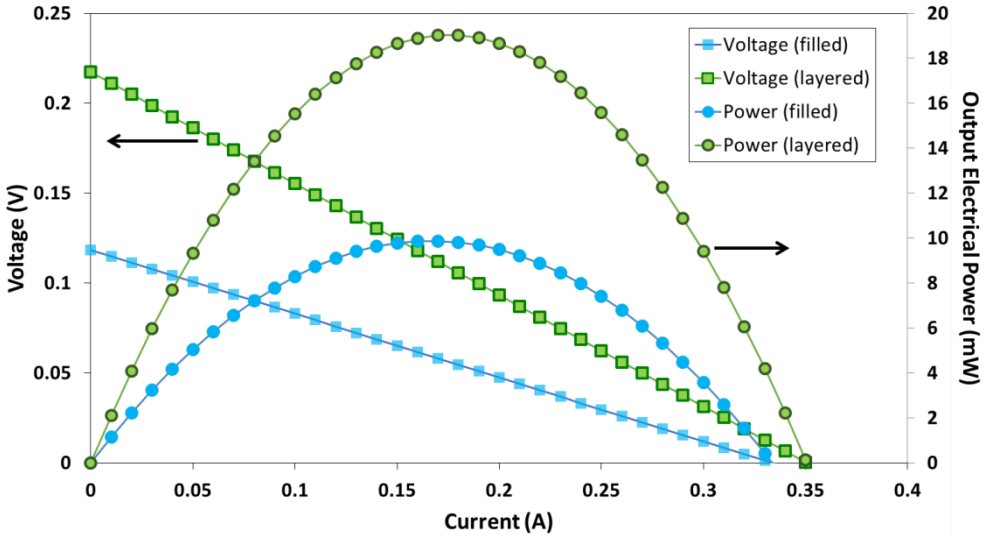

Figure 7. Open circuit voltage and output electrical power for modules with square legs of filled and layered geometries. The results are for a module modeled with HMS legs.

Figure 7 reports the output electrical voltage of the thermoelectric module as function of the electrical current through the legs, and the benefit of the layered geometry is demonstrated again. The module with layered leg geometry shows a higher V_{oc} (217 mV) than the module with the conventional legs for which the V_{oc} is 46% lower (118 mV). While the module with the layered leg geometry has a higher internal resistance (0.62 Ω) than that of the filled geometry (0.36 Ω), the power output of the former is still higher as shown in Figure 7. The peak output for the layered leg module is 19 mW which is 48% higher than the power of the filled leg module (9.9 mW). The corresponding peak areal power densities for the layered and filled legs are 39 W/m^2 and 20 W/m^2, respectively, for the 22 x 22 mm^2 module. Despite the thermal radiation between layers in the layered leg geometry, the overall temperature gradient across the entire leg remains higher with layered legs leading to higher V_{oc} and output electrical power. These results indicate legs with complex shapes such as multiple layers spaced with voids are beneficial for thermoelectric module performance.

IV. Conclusion

Simulations of both traditional and novel thermoelectric leg geometries show complex geometries (e.g., layered structures where the cross-sectional area varies along the length of the leg) can result in higher thermal resistances and output electrical power from thermoelectric modules. The results presented here point to the strong potential offered by thermoelectric legs with interior voids and hierarchical geometries. However, legs with complex geometries are difficult to achieve with traditional, subtractive manufacturing approaches. Additive manufacturing offers a solution to this technical challenge since it enables fabrication of customized parts with small, complex features. Recent work on additive manufacturing of thermoelectric materials demonstrates the potential of this fabrication approach and enables new capability and adaptability for thermoelectric technologies.

Acknowledgement

Saniya LeBlanc acknowledges support from the U.S. Department of Energy/National Nuclear Security Administration through the Capital/DOE Alliance Center (DE-NA0003858).

References

[1] A. El-Desouky, M. Carter, M. Mahmoudi, A. Elwany, and S. LeBlanc, "Influences of energy density on microstructure and consolidation of selective laser melted bismuth telluride thermoelectric powder," *J. Manuf. Process.*, vol. 25, pp. 411–417, 2017.

[2] G. S. Nolas, J. Sharp, and J. Goldsmid, *Thermoelectrics: Basic Principles and New Materials Developments*. 2013.

[3] T. M. Tritt, "Thermoelectric Phenomena, Materials, and Applications," *Annu. Rev. Mater. Res.*, vol. 41, no. 1, pp. 433–448, Aug. 2011.

[4] J. R. Sootsman, D. Y. Chung, and M. G. Kanatzidis, "New and old concepts in thermoelectric materials.," *Angew. Chem. Int. Ed. Engl.*, vol. 48, no. 46, pp. 8616–39, Jan. 2009.

[5] K. Yazawa and A. Shakouri, "Cost-efficiency trade-off and the design of thermoelectric power generators.," *Environ. Sci. Technol.*, vol. 45, no. 17, pp. 7548–53, Sep. 2011.

[6] T. J. Hendricks, S. Yee, and S. LeBlanc, "Cost Scaling of a Real-World Exhaust Waste Heat Recovery Thermoelectric Generator: A Deeper Dive," *J. Electron. Mater.*, vol. 45, no. 3, 2016.

[7] T. J. Hendricks, "Integrated thermoelectric-thermal system resistance optimization to maximize power output in thermoelectric energy recovery systems," in *Materials Research Society Symposium Proceedings*, 2014.

[8] P. M. Mayer and R. J. Ram, "Optimization of Heat Sink–Limited Thermoelectric Generators," *Nanoscale Microscale Thermophys. Eng.*, vol. 10, no. 2, pp. 143–155, Jul. 2006.

[9] M. T. Dunham, M. T. Barako, S. LeBlanc, M. Asheghi, B. Chen, and K. E. Goodson, "Power density optimization for micro thermoelectric generators," *Energy*, vol. 93, 2015.

[10] M. T. Dunham, M. T. Barako, S. LeBlanc, M. Asheghi-Roudheni, B. Chen, and K. Goodson, "Modeling and optimization of small thermoelectric generators for low-power electronics," in *ASME 2013 International Technical Conference and Exhibition on Packaging and Integration of Electronic and Photonic Microsystems, InterPACK 2013*, 2013, vol. 1.

[11] G. Snyder and T. Ursell, "Thermoelectric Efficiency and Compatibility," *Phys. Rev. Lett.*, vol. 91, no. 14, p. 148301, Oct. 2003.

[12] T. Caillat, J.-P. Fleurial, G. J. Snyder, and A. Borshchevsky, "Development of high efficiency segmented thermoelectric unicouples," in *Proceedings ICT2001. 20 International Conference on Thermoelectrics (Cat. No.01TH8589)*, pp. 282–285.

[13] M. S. El-Genk, H. H. Saber, and T. Caillat, “Efficient segmented thermoelectric unicouples for space power applications,” *Energy Convers. Manag.*, vol. 44, no. 11, pp. 1755–1772, Jul. 2003.

[14] P. H. Ngan *et al.*, “Towards high efficiency segmented thermoelectric unicouples,” *Phys. status solidi*, vol. 211, no. 1, pp. 9–17, Jan. 2014.

[15] D. T. Crane, D. Kossakovski, and L. E. Bell, “Modeling the Building Blocks of a 10% Efficient Segmented Thermoelectric Power Generator,” *J. Electron. Mater.*, vol. 38, no. 7, pp. 1382–1386, Jul. 2009.

[16] M. Gomez, R. Reid, B. Ohara, and H. Lee, “Influence of electrical current variance and thermal resistances on optimum working conditions and geometry for thermoelectric energy harvesting,” *J. Appl. Phys.*, vol. 113, no. 17, p. 174908, May 2013.

[17] M. Hodes, “Optimal Pellet Geometries for Thermoelectric Refrigeration,” *IEEE Trans. Components Packag. Technol.*, vol. 30, no. 1, pp. 50–58, Mar. 2007.

[18] D. Ebling, K. Bartholomé, M. Bartel, and M. Jägle, “Module Geometry and Contact Resistance of Thermoelectric Generators Analyzed by Multiphysics Simulation,” *J. Electron. Mater.*, vol. 39, no. 9, pp. 1376–1380, Sep. 2010.

[19] M. Freunek, M. Müller, T. Ungan, W. Walker, and L. M. Reindl, “New Physical Model for Thermoelectric Generators,” *J. Electron. Mater.*, vol. 38, no. 7, pp. 1214–1220, Jul. 2009.

[20] D. T. Crane and L. E. Bell, “Progress Towards Maximizing the Performance of a Thermoelectric Power Generator,” *2006 25th Int. Conf. Thermoelectr.*, pp. 11–16, 2006.

[21] A. Schmitz, C. Stiewe, and E. Müller, “Preparation of Ring-Shaped Thermoelectric Legs from PbTe Powders for Tubular Thermoelectric Modules,” *J. Electron. Mater.*, vol. 42, no. 7, pp. 1702–1706, Jan. 2013.

[22] D. Crane and Gentherm, “Thermoelectric waste heat recovery program for passenger vehicles,” in *U.S. Department of Energy Annual Merit Review*, 2013.

[23] S. Nishimoto, T. Kitayama, and Y. Fujisawa, “Tubular thermoelectric module,” US6096966A, 25-Jul-1997.

[24] A. K. Menon and S. K. Yee, “Design of a polymer thermoelectric generator using radial architecture,” *J. Appl. Phys.*, vol. 119, no. 5, p. 055501, Feb. 2016.

[25] A. K. Menon, O. Meek, A. J. Eng, and S. K. Yee, “Radial thermoelectric generator fabricated from n- and p-type conducting polymers,” *J. Appl. Polym. Sci.*, vol. 134, no. 3, Jan. 2017.

[26] L. E. Bell, “Efficiency thermoelectrics utilizing thermal isolation,” 27-Apr-2001.

[27] L. Bell, “Efficiency thermoelectrics utilizing convective heat flow,” 2001.

[28] A. Z. Sahin and B. S. Yilbas, “The thermoelement as thermoelectric power generator: Effect of leg geometry on the efficiency and power generation,” *Energy Convers. Manag.*, vol. 65, pp. 26–32, Jan. 2013.

[29] A. Ibrahim, S. Rahnamayan, M. Vargas Martin, and B. Yilbas, “Multi-objective thermal analysis of a thermoelectric device: Influence of geometric features on device characteristics,” *Energy*, vol. 77, pp. 305–317, Dec. 2014.

[30] S. Shittu, G. Li, X. Zhao, and X. Ma, “Series of detail comparison and optimization of thermoelectric element geometry considering the PV effect,” *Renew. Energy*, vol. 130, pp. 930–942, Jan. 2019.

[31] S. LeBlanc, “Thermoelectric generators: Linking material properties and systems engineering for waste heat recovery applications,” *Sustain. Mater. Technol.*, vol. 1–2, pp. 26–35, Dec. 2014.

[32] H. Zhang, D. Hobbis, G. S. Nolas, and S. LeBlanc, “Laser additive manufacturing of powdered bismuth telluride,” *J. Mater. Res.*, vol. 33, no. 23, pp. 4031–4039, Dec. 2018.

[33] M. J. Carter, A. El-Desouky, M. A. Andre, P. Bardet, and S. LeBlanc, “Pulsed laser melting of bismuth telluride thermoelectric materials,” *J. Manuf. Process.*, vol. 43, pp. 35–46, Jul. 2019.

[34] A. El-Desouky, M. Carter, M. A. M. A. Andre, P. M. P. M. Bardet, and S. LeBlanc, “Rapid processing and assembly of semiconductor thermoelectric materials for energy conversion devices,” *Mater. Lett.*, vol. 185, 2016.

[35] K. Wu *et al.*, “Preparation of n-type Bi_2Te_3 thermoelectric materials by non-contact dispenser printing combined with selective laser melting,” *Phys. status solidi - Rapid Res. Lett.*, vol. 11, no. 6, p. 1700067, Jun. 2017.

[36] Y. Mao *et al.*, “Non-equilibrium synthesis and characterization of n-type $Bi_2Te_{2.7}Se_{0.3}$ thermoelectric material prepared by rapid laser melting and solidification,” *RSC Adv.*, vol. 7, no. 35, pp. 21439–21445, Apr. 2017.

[37] Y. Thimont, L. Presmanes, V. Baylac, P. Tailhades, D. Berthebaud, and F. Gascoin, “Thermoelectric Higher Manganese Silicide: Synthetized, sintered and shaped simultaneously by selective laser sintering/Melting additive manufacturing technique,” *Mater. Lett.*, vol. 214, pp. 236–239, Mar. 2018.

[38] H. Zhang, S. LeBlanc, S. Wang, J. Yang, and P. Taylor, “Selective laser melting of half-Heusler thermoelectric materials,” in *Energy Harvesting and Storage: Materials, Devices, and Applications VIII*, 2018, vol. 10663, p. 12.

[39] Y. Yan, H. Ke, J. Yang, C. Uher, and X. Tang, “Fabrication and Thermoelectric Properties of n-Type $CoSb_{2.85}Te_{0.15}$ Using Selective Laser Melting,” *ACS Appl. Mater. Interfaces*, vol. 10, no. 16, pp. 13669–13674, Apr. 2018.

[40] M. Mejri, Y. Thimont, B. Malard, and C. Estournès, “Characterization of the thermo-mechanical properties of p-type (MnSi1.77) and n-type (Mg2Si0.6Sn0.4) thermoelectric materials,” *Scr. Mater.*, vol. 172, pp. 28–32, Nov. 2019.

[41] A. E. Bowley, L. E. J. Cowles, G. J. Williams, and H. J. Goldsmid, “Measurement of the figure of merit of a thermoelectric material,” *J. Sci. Instrum.*, vol. 38, no. 11, pp. 433–435, Nov. 1961.

[42] Y. Thimont, Q. Lognoné, C. Goupil, F. Gascoin, and E. Guilmeau, “Design of Apparatus for Ni/Mg2Si and Ni/MnSi1.75 Contact Resistance Determination for Thermoelectric Legs,” *J. Electron. Mater.*, vol. 43, no. 6, pp. 2023–2028, Jun. 2014.

[43] D. Zuckermann *et al.*, “Automated production of prototype modules from industrialized Half-Heusler material,” in *38th International Conference on Thermoelectrics*, 2019.